
This is an electronic reprint of the original article.
This reprint may differ from the original in pagination and typographic detail.

Alekseev, Prokhor A.; Borodin, Bogdan R.; Geydt, Pavel; Khayrudinov, Vladislav; Bespalova, Kristina; Kirilenko, Demid A.; Reznik, Rodion R.; Nashchekin, Alexey; Haggren, Tuomas; Lahderanta, Erkki; Cirlin, George E.; Lipsanen, Harri; Dunaevskiy, Mikhail S.

Effect of crystal structure on the Young's modulus of GaP nanowires

Published in:
Nanotechnology

DOI:
[10.1088/1361-6528/ac0ac7](https://doi.org/10.1088/1361-6528/ac0ac7)

Published: 17/09/2021

Document Version
Peer-reviewed accepted author manuscript, also known as Final accepted manuscript or Post-print

Published under the following license:
CC BY-NC-ND

Please cite the original version:
Alekseev, P. A., Borodin, B. R., Geydt, P., Khayrudinov, V., Bespalova, K., Kirilenko, D. A., Reznik, R. R., Nashchekin, A., Haggren, T., Lahderanta, E., Cirlin, G. E., Lipsanen, H., & Dunaevskiy, M. S. (2021). Effect of crystal structure on the Young's modulus of GaP nanowires. *Nanotechnology*, 32(38), Article 385706. <https://doi.org/10.1088/1361-6528/ac0ac7>

This material is protected by copyright and other intellectual property rights, and duplication or sale of all or part of any of the repository collections is not permitted, except that material may be duplicated by you for your research use or educational purposes in electronic or print form. You must obtain permission for any other use. Electronic or print copies may not be offered, whether for sale or otherwise to anyone who is not an authorised user.

Effect of crystal structure on the Young's modulus of GaP nanowires

Prokhor A Alekseev¹, Bogdan R Borodin¹, Pavel Geydt^{2,3}, Vladislav Khayrudinov⁴, Kristina Beshpalova^{5,3}, Demid A Kirilenko¹, Rodion R Reznik⁶, Alexey V Nashchekin¹, Tuomas Haggrén⁴, Erkki Lähderanta³, George E Cirlin^{6,7}, Harri Lipsanen⁴, and Mikhail S Dunaevskiy¹

¹ Ioffe Institute, Saint-Petersburg, 194021, Russia

² Physical Faculty, Novosibirsk State University, Novosibirsk, 630090, Russia

³ Department of Physics, LUT University, 53850 Lappeenranta, Finland

⁴ Department of Electronics and Nanoengineering, Micronova, Aalto University, 00076 Espoo, Finland

⁵ Department of Electrical Engineering and Automation, Aalto University, 02150 Espoo, Finland

⁶ St. Petersburg State University, Saint-Petersburg, 199034, Russia.

⁷ Alferov University, Saint-Petersburg, 194021, Russia.

E-mail: npoxep@gmail.com

Received xxxxxx

Accepted for publication xxxxxx

Published xxxxxx

Abstract

Young's modulus of tapered mixed composition (zinc-blende with a high density of twins and wurtzite with a high density of stacking faults) Gallium Phosphide (GaP) nanowires (NWs) was investigated by atomic force microscopy (AFM). Experimental measurements were performed by obtaining bending profiles of as-grown inclined GaP NWs deformed by applying a constant force to a series of NW surface locations at various distances from the NW/substrate interface. Numerical modeling of experimental data on bending profiles was done by applying Euler-Bernoulli beam theory. Measurements of the nano-local stiffness at different distances from the NW/substrate interface revealed NWs with a non-ideal mechanical fixation at the NW/substrate interface. Analysis of the NWs with ideally fixed base resulted in experimentally measured Young's modulus of 155 ± 20 GPa for ZB NWs, and 157 ± 20 GPa for WZ NWs, respectively, which are in consistence with a theoretically predicted bulk value of 167 GPa. Thus, impacts of the crystal structure (WZ/ZB) and crystal defects on Young's modulus of GaP NWs were found to be negligible.

Keywords: GaP, nanowire, atomic force microscopy, WZ/ZB, Young's modulus, bending

1. Introduction

III-V semiconductor nanowires (NWs) are considered very promising nanostructures for electronics, optoelectronics [1,2], and power generation [3–5]. Under optimal growth conditions, only NWs with high aspect ratio can be obtained. Because of the nanoscale diameter and high

aspect ratio, NWs sustain elastic strains up to 10% without fracture [6]. High deformation stability of NWs allows to control their electronic and optoelectronic properties by elastic strains. Particularly, for III-As (InAs, GaAs, InGaAs) NWs a 2% mechanical deformation was shown to redshift the photoluminescence position by 290 meV [7] or change NW conductivity by four orders of magnitude [8,9]. Non-

zero piezoelectric coefficients along the NW growth axis (111) in zinc-blende (ZB) and wurtzite (WZ) NWs allow enhancing characteristics of sensors [10], light-emitting diodes [11], ambient mechanical energy harvesters [5,12], photodetectors [13,14], and solar cells [15].

Due to the wide practical applicability of III-V NWs in flexible devices [16–18], it is necessary to know their Young's modulus that defines the limits of elasticity, i.e. reversible and deformational stress that can be applied to a NW [19]. However, acquisition of correct values of elasticity in NWs is associated with few major difficulties [20] related to the crystal defects in NWs [21], surface oxidation [22,23], growth orientation of NWs and crystal direction of semiconductor material specified for the measurement [24] and effect of the boundary conditions between NW and substrate or clamping platform [25,26].

Furthermore, crystal phase can affect the elastic properties of NWs [27]. Although bulk III-V semiconductors typically have cubic ZB structure, hexagonal WZ crystal phase can appear energetically favorable under the critical diameter of NW [28,29]. It is worth noting, that III-V NWs grown in [111]ZB and [0001]WZ directions should have equal Young's modulus. This follows from the approach proposed by R.M. Martin [30]. However, crystal lattice of WZ III-V NWs is deformed during growth [31], which slightly changes their bulk modulus [27].

Several major methods can be used to study the elastic moduli of NWs. Firstly, resonant oscillation method [32] can be used to register the resonant contour of the structure. However, resonant oscillation method is not relevant for inhomogeneous materials with various inclusions. Secondly, scanning electron microscopy (SEM) or transmission electron microscopy (TEM) -based visualization of the bends with control of the mechanical force can be utilized [6,33]. Finally, direct bending of NWs by an atomic force microscope (AFM) probe with registration of applied force and resulting deformation was successfully applied to GaAs [34] and InP [29] NWs. AFM-based experiments can be performed for NWs with one [35] or two clamped ends [36,37]. The boundary conditions (fixed or supported beam) strongly affect obtained Young's modulus [25,38,39]. AFM-based technique is advantageous because it enables the measurement of the loading curves at different distances from the clamped end. Analysis of the loading curves enables the determination of boundary conditions of NW on a substrate (clamped, fixed, or supported beam) [38].

GaP NWs have attracted attention due to their direct band gap in WZ structure [40] and excellent photonic characteristics, that make them useful for flexible waveguides [41] of visible light [42] or second harmonic generation [43]. However, elastic properties of GaP NWs have been poorly studied. Yashinsky et al. reported that ZB

GaP NWs have elastic moduli and failure strains consistent with bulk GaP [44], where the elastic moduli were obtained from Raman measurements of uniaxially tensed NWs.

In this report, we use the AFM-based approach [29] to study inclined ZB and WZ GaP NWs with twins and stacking faults grown on Si and graphene substrates. We analyze the impact of the defects on Young's modulus of NWs and we present a new method to study properties of growth contact between the NW and the substrate.

2. Samples and methods

2.1 Nanowire growth

Two types of inclined GaP NWs were studied. GaP NWs of the first type were grown on p-Si (111) substrates by using a gold nanoparticle-assisted vapor-liquid-solid (VLS) growth method inside a horizontal-flow metalorganic vapor phase epitaxy (MOVPE) system. The substrate was initially cleaned inside an ultrasonic bath by soaking in both acetone and isopropanol for 2 min, followed by a 2 min rinse in deionized water. After that, 40 nm diameter gold nanoparticles from a colloidal solution (BBI International, UK) were used as catalysts for the VLS growth. The Poly-L-Lysine solution was applied to the substrate for 10 s for better adhesion of nanoparticles, followed by 10 s deposition of gold nanoparticles. Prior to the growth, the substrate was annealed in situ at 650°C for 10 min under hydrogen flow to desorb surface contaminants. Growth step was started by switching on the trimethylgallium (TMGa) and tertiarybutylphosphine (TBP) sources simultaneously for 30 s at a fixed growth temperature of 550°C. The nominal V/III ratio during the growth was ~100, and the TMGa and TBP flows were 5.36 and 550 $\mu\text{mol}/\text{min}$, respectively. After the growth, only the TBP flow was kept on during the reactor cooling down to 250°C.

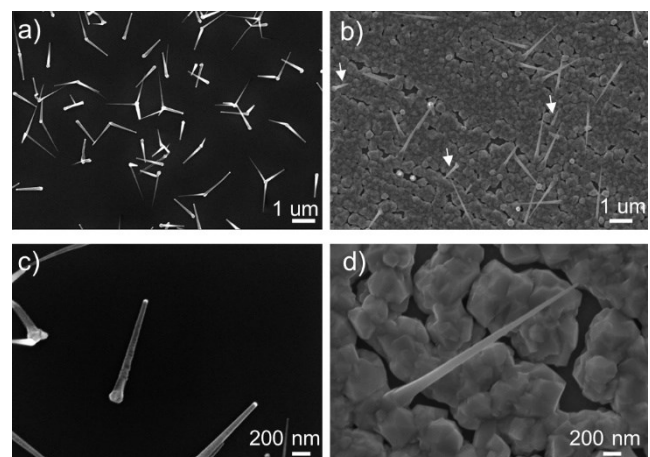


Figure 1. SEM images of GaP NWs grown by MOVPE on Si substrate (a, c) and GaP NWs grown by MBE on graphene/SiC substrate (b, d). White arrows indicate short NWs.

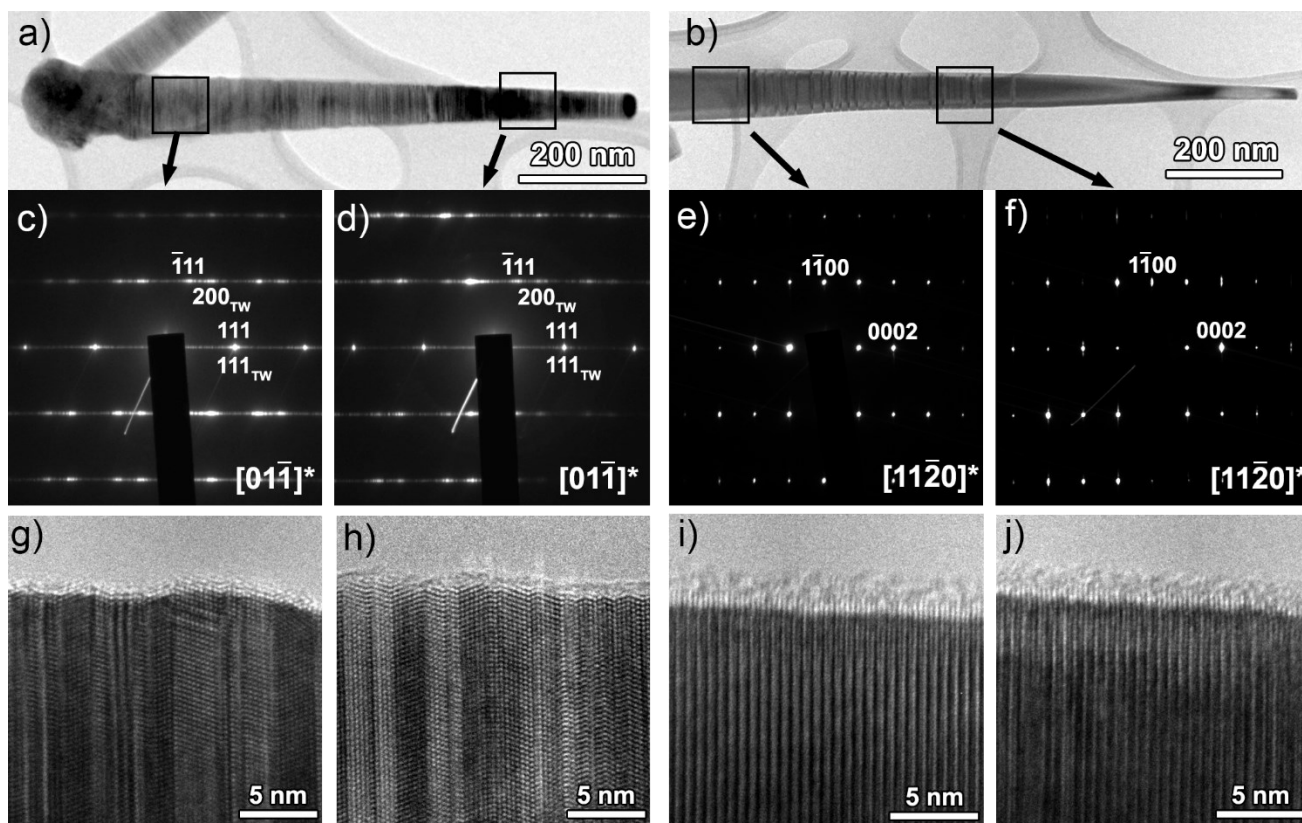


Figure 2. TEM images of the GaP NWs (a) The MOVPE-grown NW. (b) The MBE-grown NW. Black rectangles point out areas where selective area electron diffraction (SAED) patterns (c-f) and high resolution (HR) TEM images (g-j) are obtained. SAED and HRTEM images are arranged in columns below respective black rectangle. (c-d) Show the SAED that corresponds to ZB structure with a high density of twins (TW). (e-f) Show the SAED that corresponds to WZ structure.

GaP NWs of the second type were grown using molecular beam epitaxy (MBE) on SiC substrate covered by a graphene layer [45]. The growth of NWs was performed in several stages. After thermal cleaning of the substrate in metallization chamber of MBE setup “Riber Compact 21” at 500°C, Au droplets were formed on the substrate’s surface at the same temperature. Au droplets participated in growth as a catalyst for the NWs synthesis. After that, the sample was cooled down to room temperature and transferred to the growth chamber without braking ultra-high vacuum conditions. On the next stage, the substrate’s temperature in the growth chamber was increased to 500°C, then Ga and P shutters were opened, and GaP NWs were grown within 15 minutes under P-stabilized growth conditions. The flux of Ga in the synthesis of GaP NWs corresponded to the growth rate of a planar GaP layer of 2.8 Å/s. The details of the growth are presented elsewhere [46].

2.2 TEM and SEM characterization

The morphological and structural properties of the NWs were studied by scanning electron microscopy (SEM) and transmission electron microscopy (TEM). SEM

measurements were performed using Jeol JSM 7001F microscope. TEM investigations were performed using Jeol JEM-2100F microscope (accelerating voltage 200 kV, point-to-point resolution 0.19 nm). The as-grown NWs were transferred to a conventional TEM copper grid with a lacey carbon film by rubbing the latter over the substrate with the NWs.

Both types of the NWs were not intentionally doped. Obtained NWs had tapered shapes with taper angle $\alpha \sim 1$ -3 deg and inclination angle to the substrate of 23 ± 5 deg registered by the post-growth SEM (figure 1) and AFM imaging. The typical diameter of the NWs was ~ 20 -60 nm at the unfixed top parts and ~ 100 -200 nm at the bottom contact with the substrate. The lengths of the MOVPE-grown NWs were in the range of 1 - 1.5 μm (figure 1 (a, c)). The majority of NWs formed trefoils (two or three NWs grow from the same point) due to agglomeration and/or splitting of the Au catalyst particles before the growth. The lengths of the MBE-grown NWs were in the range of 1.2 - 2.6 μm (figure 1 (b, d)). A part of these NWs (marked by white arrows in figure 1(b)) indicated approximately half-lengths of the other part. The NWs had a variation of density on the substrate, which allowed us to select appropriate free-standing NWs for the study (figure 1).

The MOVPE-grown NWs had ZB crystal structure with a high density of twins. Figure 2(a) shows the corresponding TEM image and selective area electron diffraction patterns (c-d). Since a single twin defect can be considered as a WZ insert, nanowire structure can be described as a fine mixture of both WZ and ZB phases. From the high-resolution image (figure 2(g-h)) it follows that native oxide thickness does not reach 1.5 nm. The same thickness was observed for MBE-grown NWs (figure 2(i-j)). The MBE-grown NWs (figure 2(b)) had a WZ crystal structure (figure 2(e-f)) with stacking faults, mostly placed at the middle part of the NW. The average distance between stacking faults was ~ 10 nm (figure 2(j)). Chemical composition maps obtained by energy-dispersive x-ray spectroscopy of the MBE- and MOVPE-grown NWs are presented in Supplementary Information (figure S1).

2.3 AFM measurements

We used AFM-based bending profile method to perform quantitative study of the elastic moduli of GaP NWs. Details of the method are presented in our previous paper [29]. The technique allows to measure the deformation of the object by the probe with a well-controlled force (F). By analysing the deformation profiles along the NW axis it is possible to determine its stiffness and Young's modulus. Scanning probe microscopy station BRUKER Multimode 8 was used with the AFM probes BRUKER SCM-PIT. Calibration of the

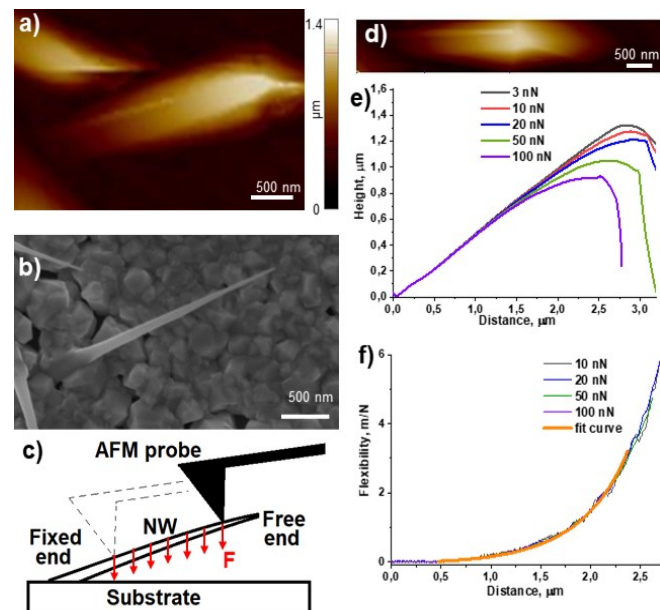


Figure 3. AFM (a) and SEM (b) images of the same MBE-grown NW with $L=2920$ nm and $R_{mid}=44$ nm. c) Schematic of NW bending by AFM probe. (d) AFM image of the GaP NW before bending experiment obtained at setpoint force of 1 nN. e) Experimental bending profiles for individual GaP NW under different setpoint forces. (f) Normalized experimental flexibility profiles $f(x) = 1/k(x)$ along the individual GaP NW with profile obtained by a fitting procedure (orange curve).

experimental setup was based on the utilization of a reference sample by the standard protocol of the quantitative nanomechanical mapping (QNM) regime of AFM. The spring constant of the AFM cantilever was measured to be 3 N/m, and the tip radius was ~ 8 nm. Firstly, we performed optical visualization to find the agglomerates of NWs on the substrate since they scatter most of the light and are visible as dark regions on the substrate. This was followed by a survey scanning by AFM with a small setpoint force and flexible probe. We combined optical, AFM and SEM (figure 3(b)) topography data to select the suitable NWs. The procedure of finding the same NWs in the AFM and SEM images is described in figure S2 in Supplementary information. The most appropriate NWs had to be standing (separated from the detached structures) with their free ends mainly oriented to the direction of the AFM cantilever (see schematics in figure 3(c)).

When the appropriate NW was found, the scan size was decreased to the size of the NW and the velocity of AFM scanning was reduced below $0.5 \mu\text{m/s}$. The angle between the AFM fast scanning direction and the projection of the neutral axis in the NW was minimized to reduce sliding. Serial recording of the *Height* (i.e. topography) and *PeakForce* (i.e. the map of the in-situ setpoint forces of probe-sample interaction) AFM data channels was done in the direction from left (bottom of the NW) to right (free end) parts of the scanned image. This was done to reduce the error associated with disturbance of the free end of the NW by the AFM probe. (can be seen in the right part of figure 3(c)). The AFM scanning had to be done with different setpoint forces in the range of 1 nN - 200 nN. Such ramping is preferable to be started from the smallest force in order to secure the studied NW from inelastic deformation. Increasing the setpoint force F resulted in intensified bending of the NW down to the substrate, which was accurately recorded into the *Height* channel (figure 3(d)). The enlarged distance from the fixed end resulted in intensified bends, although the area near the free end was typically not recorded due to parasitic lateral deformations and sliding of the AFM probe from the NW spine. When all recording parameters were optimized, it was possible to acquire the experimental data on bending profiles for further analysis.

2.4 Numerical procedure for obtaining Young's modulus

Horizontal line profiles (figure 3(e)) from the data channels of *Height* and *PeakForce* for each setpoint force F of 1 nN, 5 nN, 10 nN, 50 nN and 100 nN, were used to calculate the bending profiles $\omega_F(x)$ by the formula:

$$\omega_F(x) = \Delta\text{Height} = h_F(x) - h_0(x), \quad (1)$$

where $h_F(x)$ is the height of a scanned location x on the NW measured under the setpoint force F and $h_0(x)$ is the topographical height measured under the setpoint force that is considered negligible. We assumed the scanning force 1 nN as negligible in the present experiment. The inclination angle of the NW in figure 3(e) was ~ 27 deg.

Calculation of the bending deformation profile $\omega_F(x)$ with identified spring constant of the AFM probe enables to obtain the stiffness profile $k(x)$ of the NW. However, flexibility profiles $f(x)$ as being inversed to the stiffness profiles could be modelled without difficulties associated with infinite stiffness at the fixed end of the NW. Therefore, the measured bending profiles were recalculated into flexibility profiles $f(x)$ for the single NWs when dividing the deformation by the applied force F . Later, the flexibility profiles $f(x)$ were normalized for the same force (figure 3(f)) and analyzed with the help of the formula which is used to calculate the Young's modulus E_{mat} of the tapered NWs when the flexibility profile is known [29]:

$$f(x) = \frac{4}{3\pi} \frac{1}{E_{mat}} \frac{1}{R_{mid}^4} \frac{x^3}{(1+u(x-L/2))(1-uL/2)^3}, \quad (2)$$

where R_{mid} is the average radius of a NW, L is the length of a NW, $u = \alpha/R_{mid}$ is an auxiliary coefficient associated with the tapering angle α , and x is the coordinate of the AFM probe when deforming the NW. R_{mid} and α were obtained for each NW from SEM measurements.

Normalized flexibility coefficient profile describes deformability for all applied bending forces and represents all distances from the fixed point along a single individual NW. NWs were not detached or inelastically deformed during the bending measurements even after bending deformations in the order of 500 nm. Numerical simulation of the experimental data for the flexibility profiles $f(x)$ using the equation (2) allowed obtaining the correlating coefficient u and the value of Young's modulus E_{mat} for individual GaP NWs. Fitting of the correlating parameters was done in Origin software by the protocol described by Dunaevskiy [29]. For example, the orange line in figure 3(f) corresponds to $E_{mat}=152$ GPa. AFM bending was performed on 22 single NWs grown by MOVPE and 20 single NWs grown by MBE.

3. Results and discussion

3.1 Analysis of the mechanical boundary conditions

The flexibility profiles were initially analyzed to reveal the boundary conditions at the growth contact of each NW before the calculation of Young's modulus of GaP NWs. Figure 4 shows SEM images and flexibility profiles measured for both MOVPE (a-b) and MBE (c-d) grown NWs. The profiles were measured with applied force $F=100$

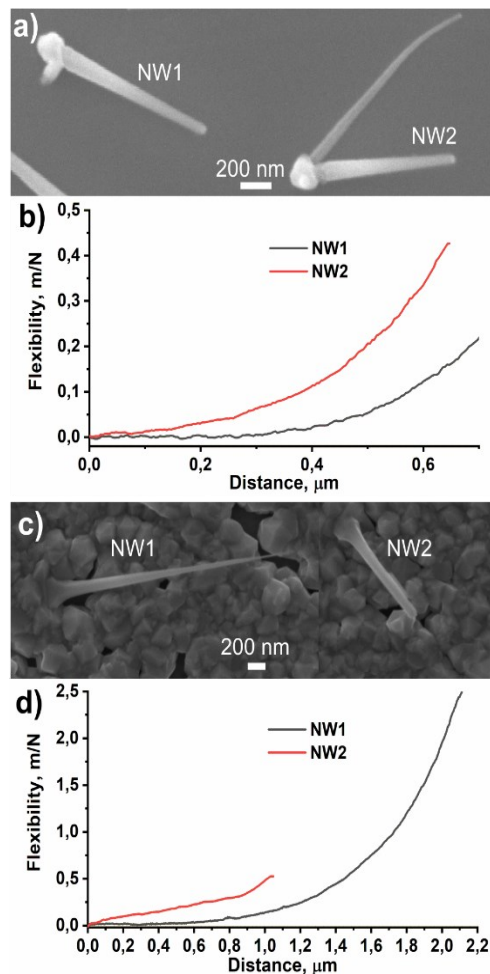


Figure 4. SEM images (a),(c) and corresponding normalized experimental flexibility profiles (b), (d) for MOVPE-grown (a-b) and MBE-grown (c-d) NWs. The size of NW1 (a) is $L=960$ nm, $R_{mid}=40$ nm and the size of NW2 (a) is $L=860$ nm, $R_{mid}=37$ nm; The size of NW1 (b) is $L=2990$ nm, $R_{mid}=30$ nm and the size of NW2 (b) is $L=1481$ nm, $R_{mid}=58$ nm.

nN. Figure 4(b, d) shows that the profiles exhibit different behavior at the NWs base. Black curves have a near-zero slope at the NW base. This behavior indicates that the contact stiffness is very high at the NW base, and NWs were not bent under applied force near their base. Thus, black curves correspond to the NWs, which can be modeled as a beam with one ideally fixed end. The red curves have a slope at the base, indicating low contact stiffness at the NW base or the imperfect fixation of the nanowire. The reduction of the NW stiffness near the base could be due to decreasing of the NW diameter at the NW/substrate interface or decreasing of the Young's modulus of the material in the NWs.

Only 9 out of 22 MOVPE-grown NWs had an ideal fixation at the NW base. It is worth noting that 10 NWs with a non-ideal fixation had a trefoil structure, i.e. they had parasitic spurs as shown in figure 1(a) and figure 4 (a) "NW1". Non-ideal fixation in MOVPE-grown NWs could be caused by the relatively small diameter of the Au catalytic seeds, which leading to an area of the growth contact

significantly smaller than the NW diameter. Contact mode AFM scanning of the MOVPE-grown NWs with high contact force resulted in detachment of the NWs from the substrate. Interestingly, no “stumps” were observed in the areas where the NWs were grown after the detaching. This observation supports the suggestion that the main reason for the non-ideal fixation of the MOVPE-grown NWs is the reduction of the NW diameter at the NW/substrate interface.

For the MBE-grown NWs, 11 out of 20 had a non-ideal fixation at the NW base. Interestingly, all measured MBE-grown NWs with a shorter length (similar to NWs marked by white arrows in figure 1(b)) exhibited a non-ideal fixation. From figure 4(c) it follows that the short NWs seem to grow from the parasitic GaP particles, which covered almost all substrate surface. AFM scanning of the MBE-grown NWs in the contact mode did not detach any of the parasitic particles from the substrate. Additionally, the diameter of the MBE-grown NWs near the base did not decrease. Thus, the reduction of the contact stiffness may be caused by the decreasing of Young’s modulus of the particles due to their highly defected structure. Further analysis was made only for the NWs with the ideally fixed end.

3.2 Young’s modulus of GaP NWs

Figure 5 shows values of Young’s moduli obtained for MOVPE and MBE-grown GaP NWs. The MOVPE-grown NW Young’s moduli is 155 ± 20 GPa and the MBE-grown NW Young’s moduli is 157 ± 20 GPa, which is consistent with the bulk value in the [111] direction of 167 GPa [44,47]. Notably, the MOVPE-grown NWs had ZB structure with high density of twinning defects, which can be ascribed as single WZ inserts. The MBE-grown NWs had WZ structure with defects (stacking faults) in the middle part of the NWs. Nevertheless, the impact of these defects on the experimentally obtained Young’s modulus appears to be negligible. As mentioned earlier, Young’s moduli of the [111] ZB and [0001] WZ GaP are equal (see Supplementary Information). Accounting the effects induced by a crystal lattice deformation during the NW growth [27], the deviation of the bulk moduli is less than 5%, which is in the range of a measurement error of our experiment. While several reports attributed the change of Young’s moduli to the native oxide shell effect [6,23], in our case, the influence of the native oxide was negligible due to its low thickness (~ 1 nm). Additionally, several other reports attributed the changes of Young’s modulus to the impact of the crystal lattice defects (stacking faults [21,29,34] and twins [33]). However, boundary conditions of the NWs were assumed to be as ideally fixed end and were not studied experimentally. Here, we show that approximately half of the measured NWs had a non-ideal “soft” fixation, which could result in underestimation of Young’s modulus value in previous methods.

4. Conclusion

We investigated Young’s modulus of GaP NWs grown by MOVPE and MBE on Si and graphene/SiC substrates using AFM-based method. The MOVPE-grown NWs had ZB structure with high density of twinning defects and the MBE-grown NWs had WZ structure with high density of stacking faults. The AFM method allowed to obtain bending profiles of inclined NWs by applying a constant force along the NW body at different distances from the growth contact NW/substrate. The AFM measurements revealed that approximately half of the measured NWs (both MBE and MOVPE-grown) had a non-ideal mechanical fixation at the growth contact (NW base). Such non-ideality may lead to underestimation of the NW Young’s modulus.

The analysis of the data obtained for the NWs with ideal fixation revealed Young’s modulus 155 ± 20 GPa for MOVPE-grown NWs and 157 ± 20 GPa for MBE-grown NWs. The results are in good agreement with a theoretically predicted value of 167 GPa for bulk GaP material. Thus, the impact of the crystal structure (WZ/ZB) or crystal defects on Young’s modulus of GaP NWs was found to be negligible. We believe that these results are essential for the correct estimations of the elastic moduli of NWs and can be practical in the design of GaP NW-based devices.

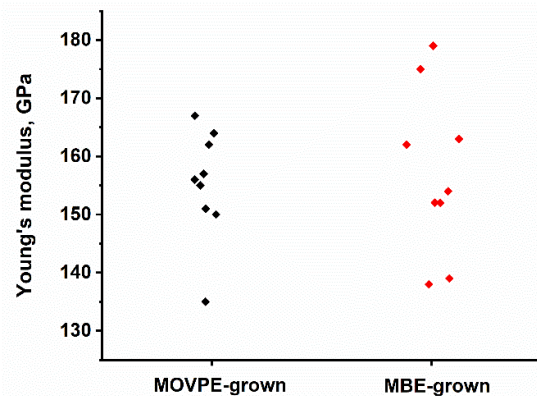


Figure 5. Young’s moduli obtained for MOVPE-grown (black) and MBE-grown (red) GaP NWs.

The presented research leaves a number of questions to be investigated in the future. It is necessary to understand the reasons for the nonideal mechanical fixing of some nanowires growing on the substrate. Additionally, a comparative study of Young’s modulus of the same nanowires by different methods (AFM bending, resonance methods, uniaxial compression with control in SEM) is in high demand.

Authors’ statement/Competing interests

The authors declare no conflict of interest.

Acknowledgments

This work is supported by Presidential Grant MK-1543.2020.2

V.K. acknowledges the support of Aalto University Doctoral School, Walter Ahlström Foundation, Elektronikkainsinöörien Säätiö and Nokia Foundation. V.K. acknowledges the provision of facilities and technical support by Aalto University at Micronova Nanofabrication Centre.

MBE growth of GaP NWs was supported by the Russian Science Foundation (Grant 19-72-30004).

SEM and TEM studies were performed using equipment of the Federal Joint Research Center “Material science and characterization in advanced technology” supported by the Ministry of Science and Higher Education of the Russian Federation (id RFMEFI62119X0021).

References

- [1] Li Y, Qian F, Xiang J and Lieber C M 2006 Nanowire electronic and optoelectronic devices *Mater. Today* **9** 18–27
- [2] Joyce H J, Gao Q, Tan H H, Jagadish C, Kim Y, Zou J, Smith L M, Jackson H E, Yarrison-Rice J M, Parkinson P, and others 2011 III–V semiconductor nanowires for optoelectronic device applications *Prog. Quantum Electron.* **35** 23–75
- [3] Krogstrup P, Jørgensen H I, Heiss M, Demichel O, Holm J V, Aagesen M, Nygard J and i Morral A F 2013 Single-nanowire solar cells beyond the Shockley–Queisser limit *Nat. Photonics* **7** 306
- [4] Åberg I, Vescovi G, Asoli D, Naseem U, Gilboy J P, Sundvall C, Dahlgren A, Svensson K E, Anttu N, Björk M T, and others 2016 A GaAs nanowire array solar cell with 15.3% efficiency at 1 sun *IEEE J. Photovolt.* **6** 185–90
- [5] Alekseev P A, Sharov V A, Geydt P, Dunaevskiy M S, Lysak V V, Cirlin G E, Reznik R R, Khrebtov A I, Soshnikov I P and Lähderanta E 2018 Piezoelectric current generation in wurtzite GaAs nanowires *Phys. Status Solidi RRL–Rapid Res. Lett.* **12** 1700358
- [6] Wang Y-B, Wang L-F, Joyce H J, Gao Q, Liao X-Z, Mai Y-W, Tan H H, Zou J, Ringer S P, Gao H-J and Jagadish C 2011 Super Deformability and Young’s Modulus of GaAs Nanowires *Adv. Mater.* **23** 1356–60
- [7] Signorello G, Karg S, Björk M T, Gotsmann B and Riel H 2013 Tuning the light emission from GaAs nanowires over 290 meV with uniaxial strain *Nano Lett.* **13** 917–24
- [8] Signorello G, Sant S, Bologna N, Schraff M, Drechsler U, Schmid H, Wirths S, Rossell M D, Schenk A and Riel H 2017 Manipulating surface states of III–V nanowires with uniaxial stress *Nano Lett.* **17** 2816–24
- [9] Alekseev P A, Sharov V A, Dunaevskiy M S, Kirilenko D A, Ilkiv I V, Reznik R R, Cirlin G E and Berkovits V L 2019 Control of Conductivity of In x Ga1–x As Nanowires by Applied Tension and Surface States *Nano Lett.* **19** 4463–9
- [10] Calahorra Y, Husmann A, Bourdelain A, Kim W, Vukajlovic-Plestina J, Boughey C, Jing Q, i Morral A F and Kar-Narayan S 2019 Highly sensitive piezotronic pressure sensors based on undoped GaAs nanowire ensembles *J. Phys. Appl. Phys.* **52** 294002
- [11] Pan C, Dong L, Zhu G, Niu S, Yu R, Yang Q, Liu Y and Wang Z L 2013 High-resolution electroluminescent imaging of pressure distribution using a piezoelectric nanowire LED array *Nat. Photonics* **7** 752–8
- [12] Jamond N, Chrétien P, Houzé F, Lu L, Largeau L, Maugain O, Travers L, Harmand J-C, Glas F, Lefeuvre E, and others 2016 Piezo-generator integrating a vertical array of GaN nanowires *Nanotechnology* **27** 325403
- [13] Tsai C-Y, Gupta K, Wang C-H and Liu C-P 2017 Ultrahigh UV responsivity of single nonpolar a-axial GaN nanowire with asymmetric piezopotential via piezo-phototronic effect: dependence of carrier screening effect on strain *Nano Energy* **34** 367–74
- [14] Sha W, Zhang J, Tan S, Luo X and Hu W 2019 III-nitride piezotronic/piezo-phototronic materials and devices *J. Phys. Appl. Phys.* **52** 213003
- [15] Alekseev P A, Sharov V A, Borodin B R, Dunaevskiy M S, Reznik R R and Cirlin G E 2020 Effect of the Uniaxial Compression on the GaAs Nanowire Solar Cell *Micromachines* **11** 581
- [16] Khayrudinov V, Remennyi M, Raj V, Alekseev P, Matveev B, Lipsanen H and Haggren T 2020 Direct Growth of Light-Emitting III–V Nanowires on Flexible Plastic Substrates *ACS Nano*
- [17] Dai X, Messanvi A, Zhang H, Durand C, Eymery J, Bougerol C, Julien F H and Tchernycheva M 2015 Flexible light-emitting diodes based on vertical nitride nanowires *Nano Lett.* **15** 6958–64
- [18] Wang C, Chien J-C, Fang H, Takei K, Nah J, Plis E, Krishna S, Niknejad A M and Javey A 2012 Self-aligned, extremely high frequency III–V metal-oxide-semiconductor field-effect transistors on rigid and flexible substrates *Nano Lett.* **12** 4140–5
- [19] Kim H, Jung U S, Kim S I, Yoon D, Cheong H, Lee C W and Lee S W 2014 Young’s modulus of ZnO microwires determined by various mechanical measurement methods *Curr. Appl. Phys.* **14** 166–70
- [20] Röhlig C-C, Niebelschütz M, Brueckner K, Tonisch K, Ambacher O and Cimalla V 2010 Elastic properties of nanowires *Phys. Status Solidi B* **247** 2557–70
- [21] Chen Y, Burgess T, An X, Mai Y W, Tan H H, Zou J, Ringer S P, Jagadish C and Liao X 2016 Effect of a High Density of Stacking Faults on the Young’s Modulus of GaAs Nanowires *Nano Lett.* **16** 1911–6
- [22] Desai A V. and Haque M A 2007 Mechanical properties of ZnO nanowires *Sens. Actuators Phys.* **134** 169–76
- [23] Chen Y, Gao Q, Wang Y, An X, Liao X, Mai Y-W, Tan H H, Zou J, Ringer S P and Jagadish C 2015 Determination of Young’s modulus of ultrathin nanomaterials *Nano Lett.* **15** 5279–83
- [24] Calahorra Y and Kar-Narayan S 2018 Piezoelectricity in non-nitride III-V nanowires: Challenges and opportunities *J. Mater. Res.* **33** 611–24

- [25] Qin Q, Xu F, Cao Y, Ro P I and Zhu Y 2012 Measuring true Young's modulus of a cantilevered nanowire: effect of clamping on resonance frequency *Small* **8** 2571–6
- [26] Wang S, Shan Z and Huang H 2017 The mechanical properties of nanowires *Adv. Sci.* **4** 1600332
- [27] Bechstedt F and Belabbes A 2013 Structure, energetics, and electronic states of III–V compound polytypes *J. Phys. Condens. Matter* **25** 273201
- [28] Glas F, Harmand J-C and Patriarche G 2007 Why does wurtzite form in nanowires of III-V zinc blende semiconductors? *Phys. Rev. Lett.* **99** 146101
- [29] Dunaevskiy M, Geydt P, Lähderanta E, Alekseev P, Haggrén T, Kakko J-P, Jiang H and Lipsanen H 2017 Young's modulus of wurtzite and zinc blende InP nanowires *Nano Lett.* **17** 3441–6
- [30] Martin R M 1972 Relation between elastic tensors of Wurtzite and Zinc-Blende structure materials *Phys. Rev. B* **6** 4546–53
- [31] Kriegner D, Panse C, Mandl B, Dick K A, Keplinger M, Persson J M, Caroff P, Ercolani D, Sorba L, Bechstedt F, and others 2011 Unit cell structure of crystal polytypes in InAs and InSb nanowires *Nano Lett.* **11** 1483–9
- [32] Poncharal P, Wang Z, Ugarte D and De Heer W A 1999 Electrostatic deflections and electromechanical resonances of carbon nanotubes *science* **283** 1513–6
- [33] Liu Z, Papadimitriou I, Castillo-Rodríguez M, Wang C, Esteban-Manzanares G, Yuan X, Tan H H, Molina-Aldareguía J M and Llorca J 2019 Mechanical behavior of InP twinning superlattice nanowires *Nano Lett.* **19** 4490–7
- [34] Alekseev P A, Dunaevskii M S, Stovpyaga A V, Lepsa M and Titkov A N 2012 Measurement of Young's modulus of GaAs nanowires growing obliquely on a substrate *Semiconductors* **46** 641–6
- [35] Barth S, Harnagea C, Mathur S and Rosei F 2009 The elastic moduli of oriented tin oxide nanowires *Nanotechnology* **20** 115705
- [36] Salvétat J-P, Bonard J-M, Thomson N, Kulik A, Forro L, Benoit W and Zuppiroli L 1999 Mechanical properties of carbon nanotubes *Appl. Phys. A* **69** 255–60
- [37] Calahorra Y, Shtempluck O, Kotchetkov V and Yaish Y 2015 Young's modulus, residual stress, and crystal orientation of doubly clamped silicon nanowire beams *Nano Lett.* **15** 2945–50
- [38] Cuenot S, Fréty C, Demoustier-Champagne S and Nysten B 2003 Measurement of elastic modulus of nanotubes by resonant contact atomic force microscopy *J. Appl. Phys.* **93** 5650–5
- [39] Chen X, Zhang S, Wagner G J, Ding W and Ruoff R S 2004 Mechanical resonance of quartz microfibers and boundary condition effects *J. Appl. Phys.* **95** 4823–8
- [40] Assali S, Zardo I, Plissard S, Kriegner D, Verheijen M, Bauer G, Meijerink A, Belabbes A, Bechstedt F, Haverkort J, and others 2013 Direct band gap wurtzite gallium phosphide nanowires *Nano Lett.* **13** 1559–63
- [41] Sharov V A, Bolshakov A D, Fedorov V V, Bruyère S, Cirlin G E, Alekseev P and Mukhin I S 2020 Deep-Subwavelength Raman Imaging of the Strained GaP Nanowires *J. Phys. Chem. C*
- [42] Trofimov P, Pushkarev A P, Sinev I S, Fedorov V V, Bruyere S, Bolshakov A, Mukhin I S and Makarov S V 2020 Perovskite–gallium phosphide platform for reconfigurable visible-light nanophotonic chip *ACS Nano* **14** 8126–34
- [43] Fedorov V V, Bolshakov A, Sergaeva O, Neplokh V, Markina D, Bruyere S, Sacerens G, Petrov M I, Grange R, Timofeeva M, and others 2020 Gallium phosphide nanowires in a free-standing, flexible, and semitransparent membrane for large-scale infrared-to-visible light conversion *ACS Nano* **14** 10624–32
- [44] Yashinski M S, Gutiérrez H R and Muhlstein C L 2017 On the origins of anomalous elastic moduli and failure strains of GaP nanowires *Nanotechnology* **28** 1–16
- [45] Davydov V Y, Usachov D Y, Lebedev S, Smirnov A, Levitskii V, Eliseyev I, Alekseev P, Dunaevskiy M, Vilkov O Y, Rybkin A, and others 2017 Study of the crystal and electronic structure of graphene films grown on 6H-SiC (0001) *Semiconductors* **51** 1072–80
- [46] Reznik R, Kotlyar K, Ilkiv I, Soshnikov I, Lebedev S, Lebedev A, Kirilenko D, Alexeev P and Cirlin G 2018 MBE Growth and Structural Properties of GaP and InP Nanowires on a SiC Substrate with a Graphene Layer *Semiconductors* **52** 1428–31
- [47] Brantley W 1973 Calculated elastic constants for stress problems associated with semiconductor devices *J. Appl. Phys.* **44** 534–5